Natural Product Betulin-Based Insulating Polymer Filler in Organic Solar Cells

Qilun Zhang,* Huotian Zhang, Ziang Wu, Chuanfei Wang, Rui Zhang, Chiyuan Yang, Feng Gao, Simone Fabiano, Han Young Woo, Monica Ek, Xianjie Liu, and Mats Fahlman*

Introduction of filler materials into organic solar cells (OSCs) are a promising strategy to improve device performance and thermal/mechanical stability. However, the complex interactions between the state-of-the-art OSC materials and filler require careful selection of filler materials and OSC fabrication to achieve lower cost and improved performance. In this work, the introduction of a natural product betulin-based insulating polymer as filler in various OSCs is investigated. Donor–acceptor–insulator ternary OSCs are developed with improved open-circuit voltage due to decreased trap-assisted recombination. Furthermore, filler-induced vertical phase separation due to mismatched surface energy can strongly affect charge collection at the bottom interface and limit the filler ratio. A quasi-bilayer strategy is used in all-polymer systems to circumvent this problem. Herein, the variety of filler materials in OSCs to biomass is broadened, and the filler strategy is made a feasible and promising strategy toward highly efficient, eco, and low-cost OSCs.

1. Introduction

Organic solar cells (OSCs) have been made great progress recently due to the innovations in device engineering, photophysics, and novel materials.[1–4] The multicomponent strategy, one of the device engineering methods to expand the absorption range and/or optimize the microstructure of the photoactive layer, has been widely employed to realize high-efficiency OSCs.[5–8] Up to date, the power conversion efficiency (PCEs) of the state-of-the-art OSCs with ternary heterojunction has approached 19%. Despite the significant improvements of PCEs, stability and cost still restrict the commercialization and industrialization of OSCs. Introduction of insulating polymers into organic electronic devices has been attracted great attention, as the low-cost materials have great potential to improve the stretchability, thermal stability, and operational or environmental stability of various organic electronic devices.[9–12]

For OSCs, insulating polymers can serve as additives (low fraction < 5%) or fillers (high fraction) to optimize the blend morphology, reduce the trap states, and suppress the radiative and non-radiative recombination in active layer.[13–19] As a solid additive, 2.5% polystyrene (PS) is used in p-7,7'-[4,4-Bis(2-ethylhexyl)-4H-silolo[3,2-b:4,5-b']dithiophene-2,6-diyl]bis[6-fluoro-4-(5'-hexyl-[2,2'-bithiophen]-5-yl)benzo[c][1,2,5]thiadiazole](DTS(FBTTh$_2$)$_2$):PC$_{71}$BM system to extend the retention time of solvent, which is beneficial for crystallization of p-DTS(FBTTh$_2$)$_2$ and the evolution of individual phases.[20] Of late, Hao and coworkers introduced polypropylene

Q. Zhang, C. Yang, S. Fabiano, X. Liu, M. Fahlman
Laboratory of Organic Electronics
Department of Science and Technology (ITN)
Linköping University
SE-60174 Norrköping, Sweden
E-mail: qilun.zhang@liu.se; mats.fahlman@liu.se

Q. Zhang, S. Fabiano, M. Fahlman
Wallenberg Wood Science Center Department of Science and Technology (ITN)
Linköping University
SE-60174 Norrköping, Sweden

The ORCID identification number(s) for the author(s) of this article can be found under https://doi.org/10.1002/solr.202200381.

H. Zhang, R. Zhang, F. Gao
Department of Physics
Chemistry and Biology (IFM)
Linköping University
SE-58183 Linköping, Sweden

Z. Wu, H. Y. Woo
Department of Chemistry
College of Science
Korea University
136-713 Seoul, Republic of Korea

C. Wang
College of Materials Science and Engineering
Ocean University of China
266100 Qingdao, P. R. China

M. Ek
Department of Fiber and Polymer Technology
School of Engineering Sciences in Chemistry
Biotechnology and Health KTH Royal Institute of Technology
10044 Stockholm, Sweden

(PP), a high crystallinity polymer, into both traditional fullerene-based systems and a high-efficiency non-fullerene acceptor (NFA) system poly[(2,6-(4,8-bis(5-(2-ethylhexyl-3-fluoro)thiophen-2-yl)-benzo[1,2-b:4,5-b']dithiophene))-alt-(5,5-(1',3'-di-2-thienyl-5',7'-bis(2-ethylhexyl)benzo[1',2'-c:4',5'-c']dithiophene-4,8-dione)]:2,2'-((2Z,2'Z)-((12,13-bis(2-ethylhexyl)-3,9-diundecyl-12,13-dihydro[1,2,5]thiadiazolo[3,4e]thieno[2'',3'':4',5']thieno[2',3':4,5]pyrrolo[3,2g] thieno[2',3':4,5] thieno [3,2-b]indole-2,10-diyl)bis(methanylylidene))bis(5,6-difluoro-3-oxo-2,3-dihydro-1H-indene-2,1diylidene)) dimalononitrile (PM6:Y6).[13] Charge recombination can be suppressed by minute quantities of PP, which ensures the efficiency in thick-film OSCs. Unlike representative solvent additives 1,8-diiodooctane (DIO),[21,22] 1-chloronaphthalene (CN),[23,24] diphenyl ether (DPE),[25,26] and recently developed volatilizable solid additives,[27–30] these insulating polymers still remain in the blend film after the device fabrication. When serving as additives, the presence of the third component in the active layer features negligible drawbacks due to the tiny ratio. However, when serving as fillers, which means at a larger ratio, the situation is much more complex due to the limitation of the bulk heterojunction (BHJ) structure. In 2016, Blom et al. illustrated the trap-dilution effect by blending dominating ratio of insulating filler polyvinyl carbazole (PVK) with conjugated polymer poly[2-methoxy-5-(2'-ethylhexyloxy)-1,4-phenylene vinylene] (MEH-PPV), which resulted in a significant improvement of trap-free electron transportation.[11] To reproduce the trap-dilution effect in OSCs, we previously used poly[(2,6-(4,8-bis(5-(2-ethylhexyl)thiophen-2-yl)-benzo[1,2-b:4,5-b']dithiophene))-alt-(5,5-(1',3'-di-2-thienyl-5',7'-bis(2-ethylhexyl) benzo [1',2'-c:4',5'-c']dithiophene-4,8-dione)]: poly{[N,N'-bis(2-octyldodecyl) naphthalene-1,4,5,8-bis(dicarboximide)-2,6-diyl]-alt-5,5'-(2,2'-bithiophene)} (PBDB-T:N2200) with dominant donor ratio in an "ideal" OSC system.[31] The insulating filler PVK has suitable surface energy and molecular weight, which ensures the network penetration inside the BHJ, instead of aggregation at the bottom contact when blending is with high ratio (<60%). Multiple filler-induced improvements have been achieved obtained including the reduction of radiative and non-radiative recombination, enhancement of mobility, area scalability, and thermal and environmental stability. Moreover, similar observations were also obtained by replacing PVK with another insulator PS, which has different miscibility between insulators and semiconductors.

Nevertheless, limitation remains. Based on our previous work, we noticed that the trap-dilution strategy strongly depends on the OSC system, both in terms of the surface energies of the individual components and the macro-phase structure of the BHJ blend composition. For instance, inserting insulator at the donor–acceptor interfaces leads to less efficient charge transfer and following suppression of exciton dissociation. While aggregation of the insulator at the interface between the active layer and electrodes hinders charge collection, which is due to the mismatch of surface energy, the application of insulator in high-efficiency OSCs needs further exploration and optimization.

In this work, an insulator copolymer betulin–terephthaloyl chloride (betulin–TPC) is selected to investigate the feasibility of filler-incorporated high-efficiency OSCs.[32,33] Betulin is a naturally abundant and hydrophobic compound, which enables further reducing the cost and enhancing sustainability in OSCs.

Although the undesirable surface energy limits the filler ratio from 5% to 20%, the forest-based material shows great potential to reduce the non-radiative open-circuit voltage (V_{oc}) loss in the high-efficiency NFA system PM6:Y6. Due to self-aggregation of betulin–TPC into separated domains, the interpenetrating network of semiconductor-rich phases can be maintained inside the BHJ. However, the presence of dense insulator domains can affect charge collection at the interface between the bottom electrode and the active layer. These results show the improvement by filler strategy in high-efficiency OSC systems and also illustrate a common problem in using the filler strategy.

2. Results and Discussion

2.1. Nanoscale Morphology Analysis for the Betulin–TPC-Incorporated Thin Films

PM6:Y6 is chosen as an ideal model system for filler-incorporated NFA OSCs due to the high efficiency and filler compatibility.[34–37] The chemical structures of the donor PM6, and acceptor Y6 with their ultraviolet photoelectron spectroscopy (UPS) spectra, are shown in the Figure S1, Supporting Information. Serving as the filler, the incorporation of betulin–TPC does not change the energy levels of the donor and acceptor as shown in the lighter area, which means that no additional energy barriers at the BHJs are introduced and no influence on exciton dissociation.

A suitable morphology with an interpenetrating network of donor and acceptor phase separation is crucial for exciton dissociation inside the filler-incorporated active layer of OSCs. The ternary blends of PM6:Y6 with increasing ratio of betulin–TPC show gradually growing macro-phase separation on the surface as observed in atomic force microscopy (AFM) images (**Figure 1**). The rougher surfaces are due to the existence of high ratio betulin–TPC filler that confines the space for the semiconductors. The clear distinction between filler and semiconductor materials illustrates the interpenetrating network phase separation of donor and acceptor can be well maintained. However, the difference in surface energies of PM6 (25.25 mJ m^{-2}) and Y6 (31.93 mJ m^{-2}) will promote a vertical phase separation and yield a more complex situation when blending with the filler (35.04 mJ m^{-2}) (Table S1, Figure S2, Supporting Information). As shown in Figure S3, Supporting Information, the bottom side of the pure PM6:Y6 blend shows similar mixed-domain-like and fibrous morphology; however, the additional 10% of betulin–TPC filler to PM6:Y6 blend causes a significant change of bottom surface to macro-domain-link and negligible fibrous morphology. This result demonstrated that betulin–TPC filler may dominate the bottom surface of ternary films, and therefore, the lack of semiconductors will play a key limiting role in electron and hole transports at the bottom side. The decreased concentration of semiconductors at the bottom surface was further confirmed by angle-resolved X-ray photoelectron spectroscopy (XPS) measurement, as increasing emission angle is very surface sensitive technique. (**Figures 2** and S3, Supporting Information). Compared to the binary film, the XPS spectra of 10% filler-incorporated ternary film show weaker feature but still clear N1s and F1s peaks. Simultaneously, C1s spectral feature contributed from the additional C–O and
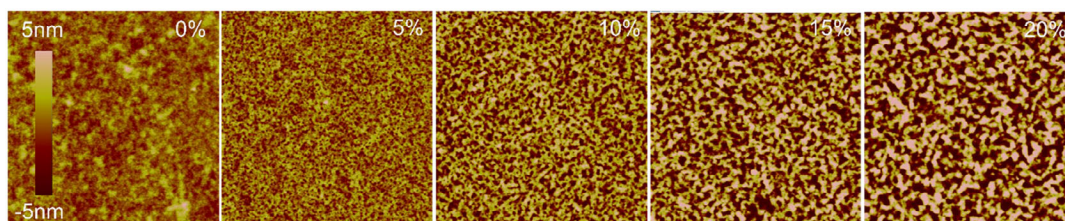
Figure 1. AFM height images (5 × 5 μm) of the poly[(2,6-(4,8-bis(5-(2-ethylhexyl-3-fluoro)thiophen-2-yl)-benzo[1,2-b:4,5-b']dithiophene))-alt-(5,5-(1',3'-di-2-thienyl-5',7'-bis(2-ethylhexyl)benzo[1',2'-c:4',5'-c']dithiophene-4,8-dione)] :2,2'-((2Z,2'Z)-((12,13-bis(2-ethylhexyl)-3,9-diundecyl-12,13-dihydro[1,2,5]thiadiazolo[3,4e]thieno[2'',3'':4',5']thieno[2',3':4,5]pyrrolo[3,2g] thieno[2',3':4,5] thieno [3,2-b]indole-2,10-diyl)bis(methanylylidene))bis(5,6-difluoro-3-oxo-2,3-dihydro-1H-indene-2,1diylidene)) dimalononitrile (PM6:Y6): betulin–terephthaloyl chloride (betulin–TPC) films with different filler concentration.
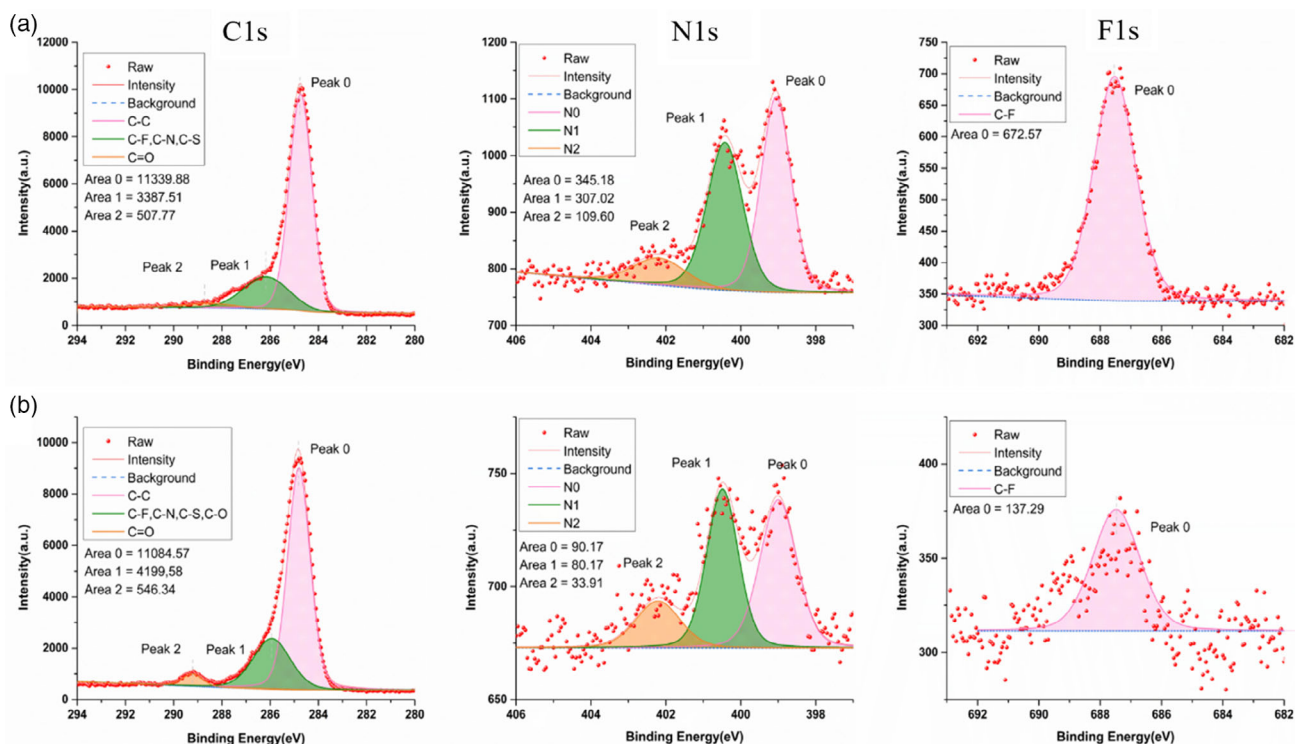

Figure 2. XPS C1s, N1s, and F1s core level spectra of the bottom surface of a) PM6:Y6 binary films and b) ternary films with 10% betulin–TPC (wt%).

C = O bond of betulin–TPC is obviously enhanced (peaks 1 and 2 in the deconvoluted C1s spectrum in the figure). The signals of N1s and F1s can also be detected in the area even closer to the surface by angle-resolved XPS measurements with the emission angle of 50 (Figure S4, Supporting Information). The charge collection efficiency is thus limited by the filler ratio as a sufficient fraction of semiconductors is needed to maintain charge transport and collection at the bottom electrode.

Furthermore, the bulk crystalline properties in BHJ films was explored by grazing-incidence wide-angle X-ray scattering (GIWAXS) (**Figures 3**a and S5, Supporting Information), and the corresponding structural parameters extracted from GIWAXS patterns are summarized in Table S2, Supporting Information. The PM6:Y6 films exhibited a preferential face-on orientation, as confirmed by a strong (010) π–π diffraction peak at the out-of-plane (OOP) direction and (100) lamellar peaks

at in-plane (IP) directions. It is worth noting that the polymer (100) diffraction and Y6 (110) diffraction are merged together. The π–π stacking from PM6 and Y6 are also overlaid, but it's reported that the strong diffraction peak in the OOP direction is associated with the π–π stacking of Y6, since the pure PM6 film presents weaker π–π peak in a smaller q_z.[34] The crystallinity of the thin films can be quantitatively investigated by the crystallites' coherence length (CCL) of the (010) peak. For the ternary film, 10% betulin–TPC decreases the CCL value from 23.26 Å (PM6:Y6) to the lower value of around 22.61 Å, whereas the π–π stacking distance is slightly increased as seen from the weak scattering peak located at a smaller q_z. The shift of (010) peak means that the Y6 dominated π–π stacking in the ternary film is slightly weaker after incorporated with betulin–TPC. The lamellar stacking distance (100) both in binary and ternary blend films are slightly increased but still similar, whereas the lamellar
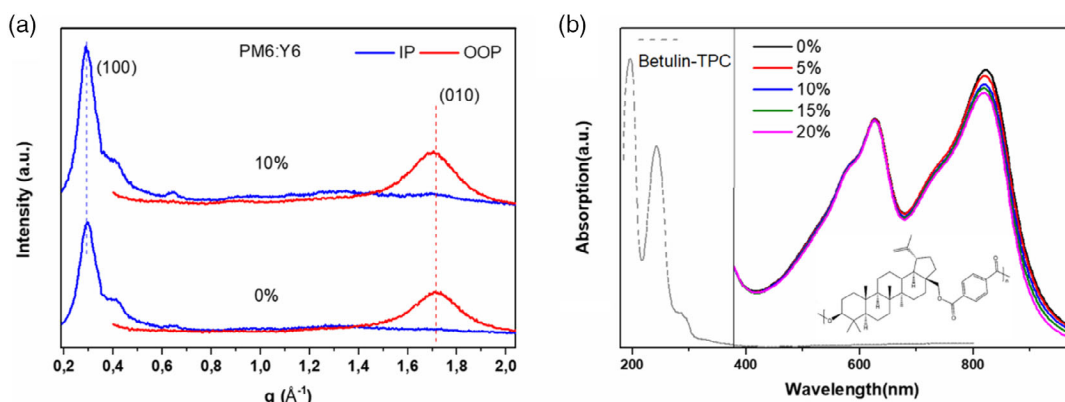
Figure 3. a) The 2D grazing-incidence wide-angle X-ray scattering (GIWAXS) patterns of binary and ternary PM6:Y6 films with 10% betulin–TPC (wt%) and b) absorption spectra of binary and ternary quasi-bilayer films with different concentration of betulin–TPC. The insertion is the chemical structure of betulin–TPC.

CCL are also increased, implying an increased lamellar crystalline size. These results indicate that the additional betulin–TPC filler is not favorable for the π–π stacking of Y6 in BHJ films, but overall the crystallinity of the BHJ films is still well kept.

The influence of the introduction of betulin–TPC on the optical properties of the active layer of the OSCs is further investigated by ultraviolet visible absorption (UV–vis) spectroscopy (Figure 3b). As all active layers have very similar thickness, the addition of a filler fraction inside the active layer obviously causes a reduced intensity of absorption. The nearly identical 0–0/0–1 peak ratio of PM6 indicates the intermolecular π–π stacking for the ternary blends is well kept with up to 20% betulin–TPC. It is worth noting that the absorption of betulin–TPC is mainly at the UV region (Figure 3b), ensuring that the betulin–TPC filler neither acts as light absorber nor charge traps inside the active layer.

2.2. Photovoltaic Performance, Electrical Properties, and Stability

Although the necessary interpenetrating donor/acceptor network for charge transport is maintained, the threshold of filler ratio is limited by the charge collection on the bottom electrode. We now evaluate its influence on key photovoltaic parameters in OSCs based on a conventional architecture of indium tin oxide (ITO)/poly(3,4-ethylenedioxythiophene) polystyrene sulfonate (PEDOT:PSS)/active layer/N,N'-Bis{3-[3-(Dimethylamino) propylamino]propyl}perylene-3,4,9,10-tetracarboxylic diimide (PDINN)/Ag. The active layers have negligible thickness difference from 105 to 95 nm with increasing filler ratio. The current density–voltage (J–V) characteristics of OSCs are displayed in **Figure 4**a and the detailed photovoltaic parameters are listed in **Table 1**. Compared to the standard device with pure PM6: Y6 active layer, the filler-incorporated devices show gradual change in V_{oc} and fill factor (FF) with increasing filler ratio. Since there is no change in the optical bandgap of donor and acceptor in the BHJ upon filler, the reduction of short-circuit current (J_{sc}) may come from decreased absorption or decreased

charge dissociation. To further understand the influence of betulin–TPC filler on the charge dynamics of the BHJ system, we measured the field (V_{eff}) dependence of photocurrent density (J_{ph}). The J_{ph} quickly saturates for $V_{eff} > 1$ V for all conditions (Figure S6a, Supporting Information). As shown in Figure 4b, we calculated the charge extraction probability P(E,T) in the OSCs to evaluate the exciton-to-charge generation and charge extraction properties of the blend films by normalizing J_{ph} with respect to J_{sat} (J_{ph}/J_{sat}).[38] P(E,T) values (η_{diss}) under short-circuit conditions for all the devices were kept about 98%, which confirms that absorption decrease is the main reason of photocurrent decrease. However, P(E, T) (η_{coll}) at the maximum power point (Mpp) decreases, especially when the filler ratio is higher than 10%. The reduction of charge collection probability is consistent with the reduced FF obtained from the J–V characteristics, which indicates the increased filler concentration at the bottom electrode that blocks the charge collection is the main reason for the decreased photovoltaic performance.

The relations between J_{sc} or V_{oc} and light intensity (P_{light}) are further investigated to explore the charge recombination in filler-incorporated devices.[39–41] As shown in Figure 4c, the calculated slope α in the power-law dependence ($J_{sc} \propto P_{light}{}^{\alpha}$) is closer to unity, which depicts bimolecular recombination is similar and weak in both situations. In addition, the slope of $nkT q^{-1}$ in the function of $V_{oc} \propto nkT q \ln P^{-1}$ (k is Boltzmann constant, q is elementary charge, and T is temperature) is an indicator of the competition between trap-assisted recombination ($n = 2$) and bimolecular recombination ($n = 1$), which could be extracted by plotting V_{oc} versus the natural logarithm of P_{light}, as shown in Figure 4d. The comparable fitted slopes of binary and ternary devices are around 1.27 and 1.17 at moderate intensities, respectively. This demonstrates that the bulk recombination is still dominated by bimolecular pathways and that the filler material can suppress trap-assisted recombination. Filler-suppressed trap-assisted recombination is also reflected by the n transition at low light intensity. Specifically, the V_{oc} of binary device quickly drops at low light intensity showing a nonlinear region with an increasing n form 1 to above 2. This is typical for trap-limited transport. On the contrary, the ternary device with filler can keep an
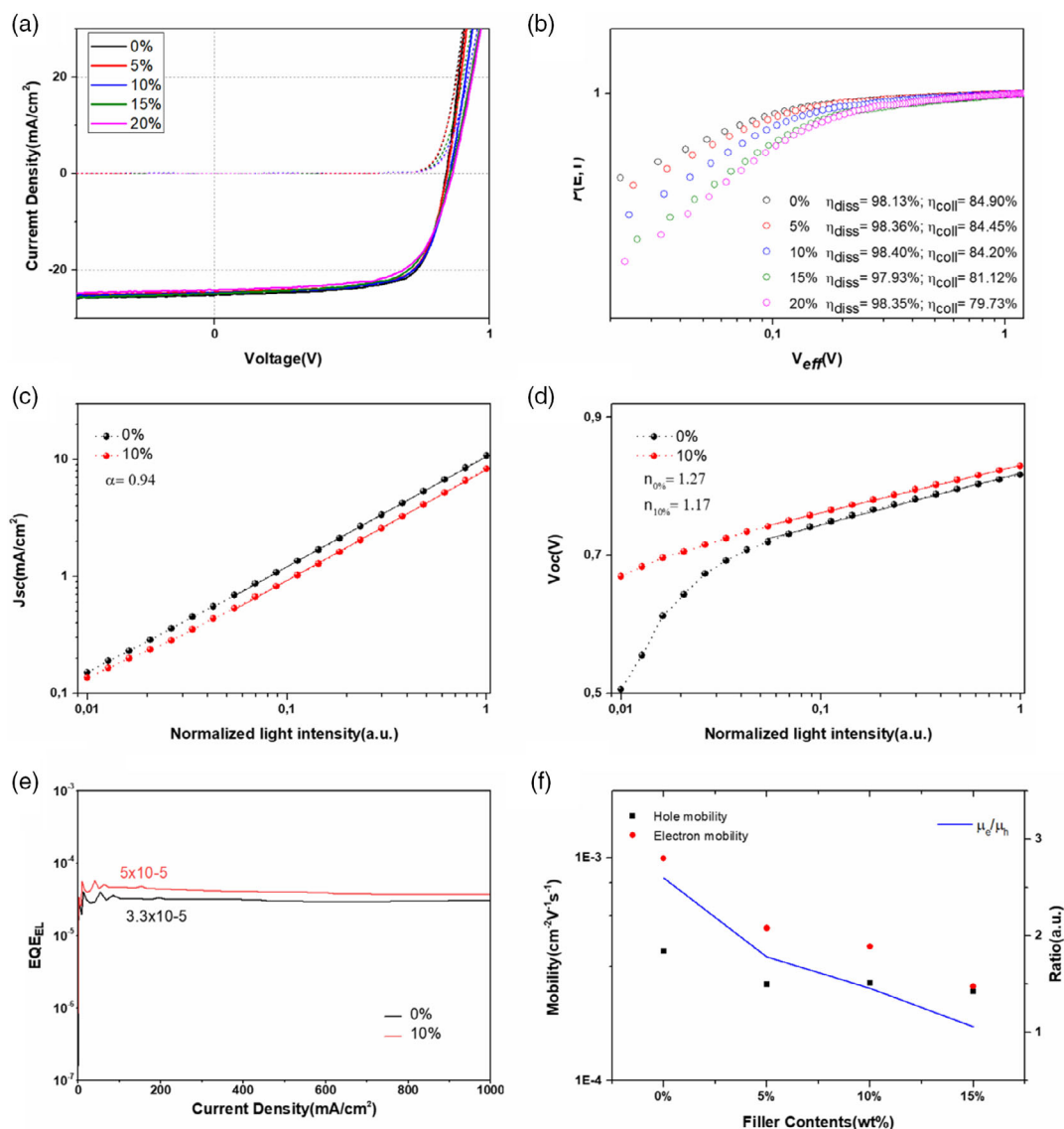
Figure 4. a) Current density–voltage (*J–V*) curves and b) P (E, T) versus voltage curves of PM6:Y6 organic solar cells (OSCs) with different concentration of betulin–TPC. Light intensity-dependent c) short-circuit current (*J*sc) and d) open-circuit voltage (*V*oc) characteristics of PM6:Y6 solar cells with or without 10% betulin–TPC (wt%). e) EQE_EL values of the corresponding OSCs. f) Hole, electron mobility, and the ratio of μ_e/μ_h of PM6:Y6 binary and ternary films with different concentration of betulin–TPC.

Table 1. Summarized photovoltaic performance parameters of PM6:Y6 OSCs fabricated with and without different concentration of betulin–TPC.

Ratio	V_{oc} [V]	J_{sc} [mA cm^{-2}]	FF	PCE
0%	0.84	25.2	71.2%	15%
5%	0.845	24.5	70.6%	14.6%
10%	0.855	24.7	69.6%	14.7%
15%	0.858	24.9	66.7%	14.2%
20%	0.865	24.2	65.1%	13.6%

approximate linear curve of V_{oc} at the same light intensity and the slope indicates only a weak dependence on traps. Because the

V_{oc} increase strongly depends on the ratio of filler despite no change in the transport gap or the optical bandgap of the active materials, we assume that the decreased V_{oc} loss corresponds to decreased trap-assisted recombination. The nonradiative voltage loss (ΔV_{nr}) can be obtained independently by quantum yield of the electroluminescent emission (EQE_EL) measurement in Figure 4e, which shows the decreased value by 10 mV with additional 10% of betulin–TPC filler.[42] The V_{oc} loss analysis is shown in the supporting information (Figure S7 and Table S3, Supporting Information).

To further investigate the charge transport dependence on filler concentration, charge-carrier mobilities were examined from space charge limited current (SCLC) in single-carrier devices, as shown in Figure 4f (Figure S8, Supporting

Information). The electron (μ_e) and hole (μ_h) mobilities are both decreased with the increasing of filler ratio, which can be assigned to the increased filler concentration at the bottom side. Interestingly, the hole mobility decrease has weaker correlation with the filler ratio, which will result in more balanced electron and hole mobility μ_e/μ_h from 2.60 to 1.05 with increasing ratio of betulin–TPC filler. Although the decreased mobility in total will limit the device performance, the balanced charge mobility facilitates the electron and hole transport in filler-incorporated OSCs.

The thermal stability of the OSCs was tested at different temperatures. As shown in **Figure 5**, the binary device without filler shows significant drops for all the photovoltaic parameters with the increasing temperature. The performance drops are suppressed with increasing filler ratio, especially for V_{oc} and J_{sc}, with the final values maintained at 43% which is 2 and 3 times higher than the values of pure binary device after 180 °C heating, respectively. The suppressed decrease of V_{oc}, J_{sc}, and FF results in a huge contrast in PCE which can be 9–10 times when the filler ratio is larger than 10%. We speculate that the improved thermal stability for the filler-incorporated devices are caused by a more resilient morphology induced by the composite effect of the filler, as shown in Figures S10 and S11, Supporting Information. It's worth noting that unlike our previous work in PBDB-T:N2200 system, the thermal degradation is significantly stronger in this work. One plausible explanation may be from the degradation between the acceptor Y6 and the cathode interface layer PDINN under high temperature. Similar degradation can be also observed in the electron-only device, and the electron mobility for all the devices is decreased in two orders with the thermal stress.

In contrast, the hole mobility as shown in the hole-only devices is kept at the same order of magnitude under 180 °C.

2.3. Quasi-Bilayer Strategy Based on PBDB-T/N2200

With the successful application of betulin–TPC filler in the PM6: Y6-based OSCs, we further studied the filler for OSCs that feature severe filler–semiconductor surface energy incompatibility. The chemical structures of the donor PBDB-T, and acceptor N2200 with their UPS spectra, are shown in the Figure S1, Supporting Information. Betulin–TPC has a similar surface energy to PVK, which indicates it will also tend to aggregate at the bottom of the blend film. However, the smaller average molecular weight ($M_w = 9$ KDa) and relatively large polydispersity index (PDI = 3.1) will make the low-molecular mass betulin–TPC more likely to go through the film to the bottom side. As a result, the stronger vertical phase separation between betulin–TPC and semiconductors could totally block the transport channel for electrons and holes.

A quasi-bilayer strategy is applied to solve this problem. Benefiting from the limited solubility of N2200 in chloroform, a quasi-bilayer OSC device with an inverted configuration of ITO/ZnO nanoparticles /N2200/PBDB-T:betulin–TPC/MoO3/Ag can be successfully fabricated. The robust N2200 film is expected to prevent the betulin–TPC filler from forming a dense insulator layer between the bottom electrode and the active layer. The J–V characteristics of OSCs are displayed in **Figure 6**a and the detailed photovoltaic parameters are listed in Table S5, Supporting Information. With increasing filler ratio from 0% to 10%, the
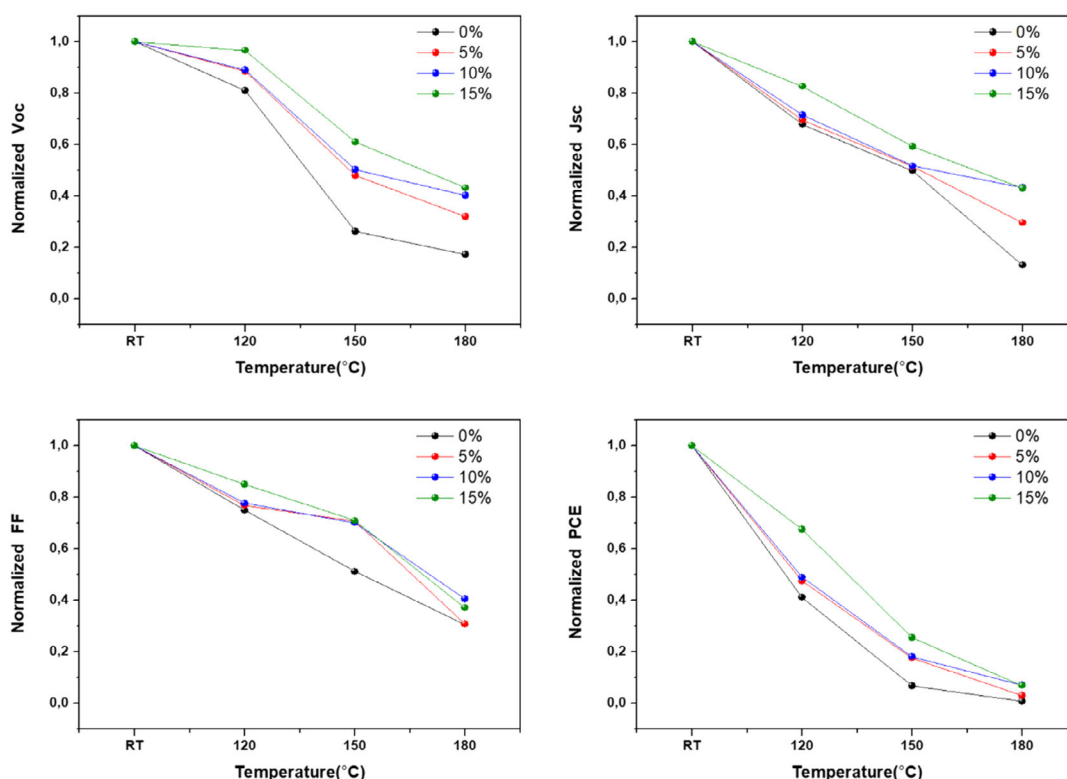

Figure 5. Degradation of photovoltaic parameters of PM6:Y6 OSCs with different filler ratio under various of temperatures.
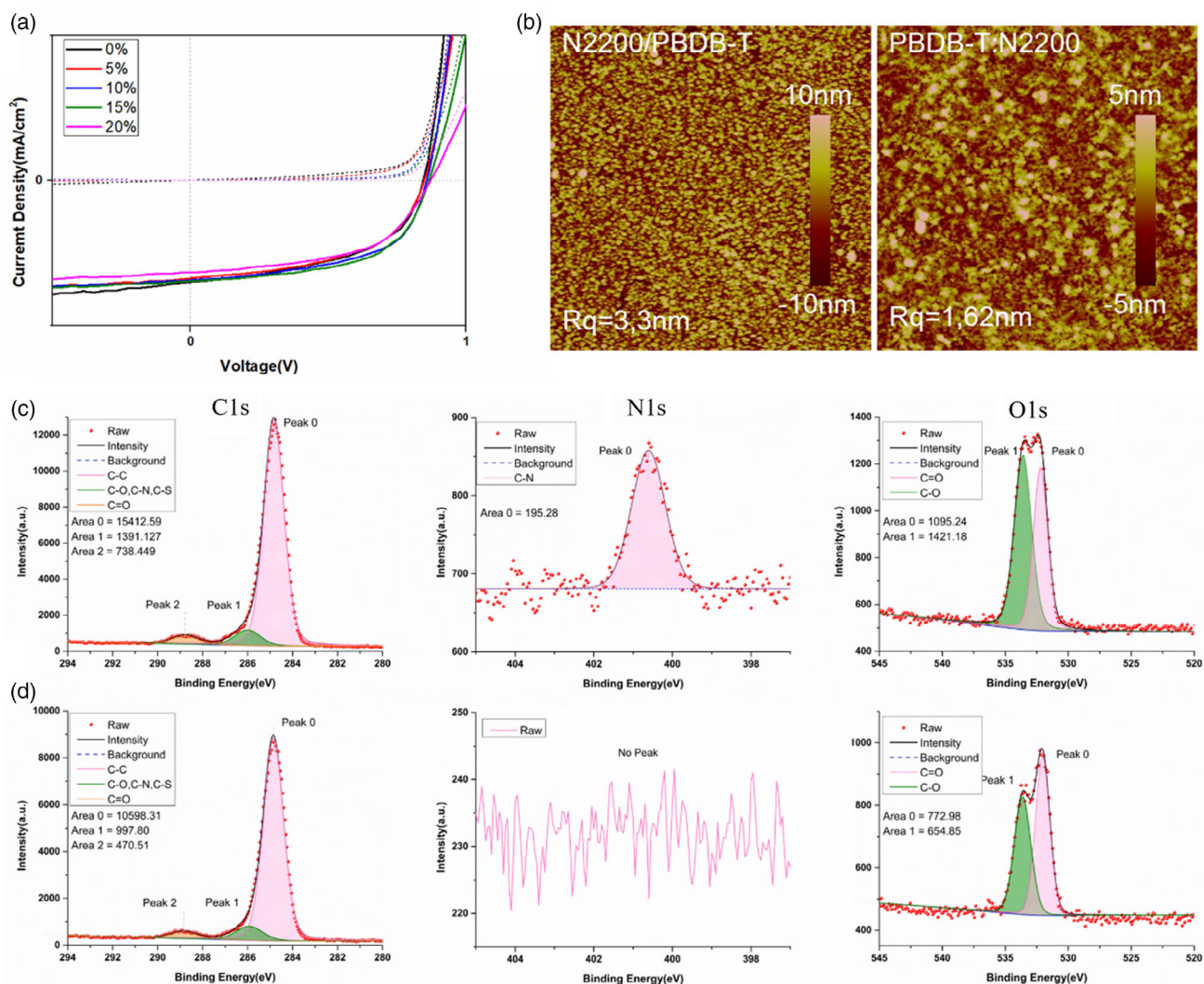
Figure 6. a) J–V curves of poly[(2,6-(4,8-bis(5-(2-ethylhexyl)thiophen-2-yl) -benzo[1,2-b:4,5-b']dithiophene))-alt-(5,5-(1',3'-di-2-thienyl-5',7'-bis(2-ethyl-hexyl) benzo [1',2'-c:4',5'-c']dithiophene-4,8-dione)]: poly{[N,N'-bis(2-octyldodecyl) naphthalene-1,4,5,8-bis(dicarboximide)-2,6-diyl]-alt-5,5'-(2,2'-bithiophene)} (N2200/PBDB-T) quasi-bilayer OSCs with different concentrations of betulin–TPC. b) AFM height images (5 × 5 μm) of the bottom side of the quasi-bilayer and blend films with 10% betulin–TPC (wt%). XPS C1s, N1s, and F1s core level spectra of the bottom surface of c) N2200/PBDB-T quasi-bilayer films and d) blend ternary films with 10% betulin–TPC (wt%).

V_{oc} and FF gradually increase until reaching a V_{oc} threshold at the ratio of 15%. Here, the FF starts to drop, and the V_{oc} and FF drop becomes significant when the ratio is above 20%. The J_{sc} is slightly fluctuating, which may result from the ununiform penetration of PBDB-T into N2200 when incorporated with betulin–TPC filler.

The increasing betulin–TPC ratio will cause increased macro-phase separation, which is similar to PM6:Y6 (Figure S12, Supporting Information). However, the bottom surfaces of the blend and quasi-bilayer films incorporated with 10% betulin–TPC show totally different morphology. As shown in Figure 6b, the blend film shows smoother bottom surface, but a similar morphology cannot be observed from the quasi-bilayer film bottom surface AFM image. The XPS spectra show the elemental structure of the respective bottom surfaces (Figure 6c,d). Compared to the PBDB-T:N2200 film, the ternary blend film shows no peak in N1s region, suggesting that the bottom side is completely dominated by betulin–TPC. The strong signal of O1s double peaks and peak 2 of C1s has similar binding energy and shape compared to those of pure betulin–TPC (Figure S4c, Supporting Information). On the contrary, the quasi-bilayer N2200/PBDBT:betulin–TPC film shows a clear N1s peak, unbalanced intensity of O1s peaks, and a boarder peak 2 feature with shifted binding energy to higher in C1s, which corresponds to a N2200 and betulin–TPC mixture at the bottom side. The calculated ratio of N2200 to betulin–TPC is about 3:1 by using the relative intensity of the C1s and N1s peaks. The XPS spectra correlate with the observed AFM results. Unlike the pure PBDB-T:N2200 films with fibrous morphology, the quasi-bilayer and blend films with betulin–TPC show relatively rougher mixed-domain-like and smooth dense morphology, respectively.
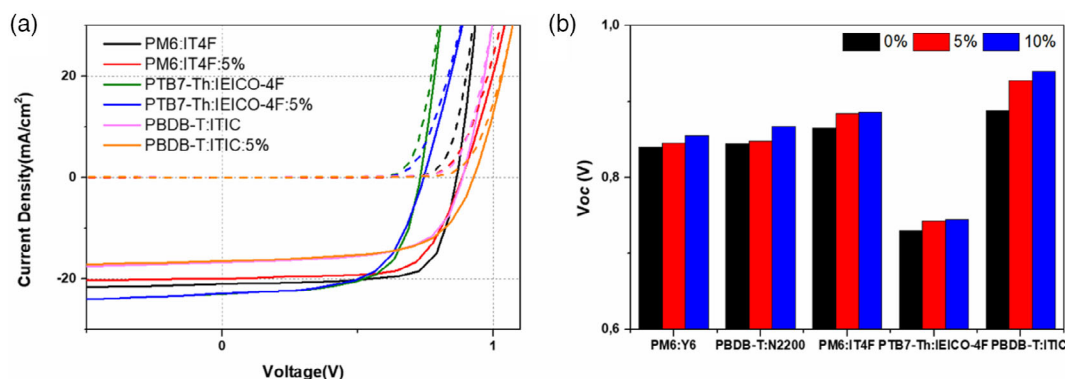
Figure 7. a) *J–V* curves of different OSCs with and without 5% betulin–TPC (wt%). b) Summarized betulin–TPC concentration-dependent *V*$_{oc}$ increasing among various of OSCs in this work.

The UV–Vis absorption and GIWAXS data of the PBDB-T:N2200 system are consistent with the trend of the PM6:Y6 system, that is, good crystallinity of the BHJ films and relatively undisturbed short-range intermolecular π–π stacking. (Figure S13, Supporting Information).

2.4. Use of Other NFA Systems

Our results have clearly demonstrated that betulin–TPC is able to suppress *V*$_{oc}$ loss of PM6:Y6 blend and N2200/PBDB-T quasi-bilayer systems. To investigate the universality of betulin–TPC filler, this method is also utilized in the other NFA systems, such as PM6:9-bis(2-methylene-((3-(1,1-dicyanomethylene)-6,7-difluoro)-indanone))-5,5,11,11-tetrakis(4-hexylphenyl)-dithieno[2,3-d:2′,3′-d′]-s-indaceno[1,2-b:5,6-b′]dithiophene (IT4F), poly([2,6′-4,8-di (5-ethylhexylthienyl)benzo[1,2-b;3,3-b]dithiophene]{3-fluoro-2[(2-ethylhexyl)carbonyl]thieno[3,4-b]thiophenediyl}) (PTB7)-Th: 2,2--((2Z,2-Z)-(((4,4,9,9-tetrakis(4-hexylphenyl)-4,9-dihydro-sinda-ceno[1,2-b:5,6-b′]dithiophene-2,7-diyl)bis(4-((2-ethylhexyl)oxy) thiophene-5,2-diyl))bis(methanylylidene))bis(5,6-difluoro-3-oxo-2, 3-dihydro-1H-indene-2,1-diylidene))dimalononitrile (IEICO-4F), and PBDB-T:2,2′-[[6,6,12,12-tetrakis(4-hexylphenyl)-6,12-dihy drodithieno[2,3-d:2′,3′-d′]-s-indaceno[1,2-b:5,6-b′]dithiophene-2, 8-diyl]bis[methylidyne(3-oxo-1H-indene-2,1(3H)-diylidene)]]bis [propanedinitrile] (ITIC). The device data are summarized in Table S6, Supporting Information, and *J–V* curves are depicted in **Figure 7**a. With the help of 5% of betulin–TPC, all the three ternary OSCs present enhanced *V*$_{oc}$ compared to the binary devices. The suppressed trap-assisted recombination can be found in the three systems as shown in light intensity-dependent *V*$_{oc}$ (Figure S14, Supporting Information). Similar to PM6:Y6 OSCs, the binary devices show a sharp drop of *V*$_{oc}$ at low light intensity with increasing n from 1 to above 2, whereas the ternary devices show a delayed and slight increase in n with decreasing of light intensity. The FF drops with the incorporation of betu-lin–TPC, which agrees well with that of the PM6:Y6 device. However, these systems are more sensitive to betulin–TPC, and even 10% of betulin–TPC will cause dramatic FF drop in all blend-based OSCs (Figure S15, Supporting Information). We assume that the higher boiling point solvent chlorobenzene and the usage of additives are the main reason. The increased

evaporation time during the spin-coating process will give more chances for the betulin–TPC to go through the film and aggregate at the bottom. Despite the drawbacks, betulin–TPC can serve as a filler material to suppress the *V*$_{oc}$ loss in different OSCs as shown in Figure 7b.

3. Conclusion

In summary, by utilizing the diluted organic semiconductor strategy, a copolymer of the naturally abundant and hydrophobic compound betulin is deployed as the insulator filler in OSCs. An improvement of *V*$_{oc}$ due to reduced trap-assisted recombination is demonstrated in a variety of OSCs. Simultaneously, we find that the mismatched surface energy of the filler material will negatively affect charge collection at the bottom interface where the filler aggregates, resulting in decreased FF in the OSCs, especially for the all-polymer systems. To suppress the undesirable vertical phase separation that causes FF loss, a quasi-bilayer strategy is successfully employed in the all-polymer systems. Our work suggests that the filler strategy in OSCs should be further explored and optimized, from the aspect of filler material selection (surface energy and molecular weight) and from the device fabrication process.

4. Experimental Section

Photoelectron Spectroscopy: The neat thin films (30–50 nm) of organic semiconductors were spin-coated in glove box on the substrates of UV–ozone-treated Au and Al/AlO$_x$, and then directly and quickly transferred into the load lock chamber of the ultrahigh vacuum (UHV) system for the following steps. The BHJ films were spin-coated using the same conditions as the OSCs. For the film bottom surface characterization, the thin films were spin-coated on ITO/PEDOT:PSS substrate. Then, ITO/PEDOT:PSS/organics samples were immersed in deionized water, and the separated, floated semiconductor films were flipped over and transferred onto ITO substrates, and then allowed to dry. All the neat films were not thermally annealed. All the substrates were routinely cleaned through sonication in detergent, followed by sequential washing in deionized water, acetone, and 2-propanol. The UPS experiments were done in a home-designed spectrometer, the excitation source was monochromatic He I radiation with photon energy of 21.22 eV. The work function was derived from the secondary electron cutoff and the vertical IP from the

frontier edge of the occupied density of states with an error margin of ± 0.05 eV. XPS was performed with a Scienta-200 hemispherical analyzer using monochromatized Al Kα source with photon energy of 1486.6 eV. All photoelectron spectroscopy measurements were carried out with a base pressure lower than 1×10^{-9} mbar.

Water Contact Angle Measurement: Water contact angle was measured on spin-coated neat films of corresponding material by Ossila contact angle goniometer using deionized water and ethylene glycol (EG).

AFM Measurement: AFM measurements were performed with a dimension 3100 system using antimony-doped silicon cantilevers in tapping mode.

UV–Vis Measurement: UV–vis absorption spectra were measured with a Perkin Elmer Lambda 900 UV–vis–near infrared radiation absorption spectrometer.

GIWAXS Measurement: GIWAXS measurements were performed at Beamline 9 A at the Pohang Accelerator Laboratory in South Korea. The X-ray energy was 11.07 KeV, and the incidence angle was 0.12°. Samples were measured in vacuum and the total exposure time was 10 s. The scattered X-rays were recorded by a charge-coupled device detector located 221.7788 mm from the sample. The samples for GIWAXS measurement were fabricated on silicon substrates using the same recipe for the device.

OSC Fabrication and Characterization: The OSC device with normal structure is Glass/ITO/PEDOT:PSS/Active layer/PDINN/Ag. The precleaned ITO substrate with the same procedure mentioned in photoelectron spectroscopy measurement was treated with UV–ozone for 20 min. The anode buffer layer PEDOT:PSS (Baytron P VP Al 4083) was spin-coated onto ITO-coated glass substrates, followed by annealing at 120 °C for 20 min to remove the water. The thickness of the PEDOT:PSS layer was around 35 nm, as determined by a Dektak 6M surface profilometer. The active layer solutions were prepared differently for all the systems mentioned. Specifically, PM6:Y6 mixed solution was made with a concentration of 16 mg mL^{-1} and a mass ratio of 1:1.2 in chloroform, PM6:IT4F, PBDB-T:ITIC, and PTB7-Th: IEICO-4 F mixed solution were made with a concentration of 20 mg mL^{-1} and a mass ratio of 1:1 in chlorobenzene. Before use, betulin–TPC solution was added into active layer solutions with the various of volume ratio to the host solvent, the solvent, and concentration of betulin–TPC was same to the host solution. And meanwhile, 0.5% DIO was added into PM6:IT4F and PBDB-T:ITIC solution, 4% CN was added into PTB7-Th:IEICO-4F solution. All the solutions were spin-coated directly to achieve 100 nm thickness. Thermal annealing at 110 °C for PM6:Y6, and at 100 °C for PM6:IT4F, PBDB-T:ITIC were carried out for 10 min. After deposited with about 8 nm PDINN, Finally, the coated substrates were directly transferred to a vacuum deposition system mounted inside of the glove box. The cathode Ag (100 nm) was thermally evaporated via a shadow mask under vacuum at 3×10^{-7} mbar. The inverted structure is Glass/ITO/ZnO/N2200/PBDB-T: betulin–TPC/MoO$_3$/Ag. For the cathode buffer layer, ZnO nanoparticle (N10, Avantama) was spin-coated onto ITO-coated glass substrates with 3000RPM, followed by annealing at 120 °C for 20 min to achieve the thickness about 30 nm. PBDB-T and N2200 were separately dissolved by chloroform and chlorobenzene with a concentration of 5 mg mL^{-1}, and N2200/PBDB-T quasi-bilayer films were fabricated by sequential deposition (SD) method. The films were annealed at 100 °C for 10 min, after that, MoO$_3$ (8 nm) and Ag (100 nm) were thermally evaporated via a shadow mask under vacuum at 3×10^{-7} mbar. The effective device area was 0.043 cm^2. *J–V* characteristics were recorded by a Paios platform under illumination of an AM1.5 solar simulator with an intensity of 100 mW cm^{-2} in the glove box. The light intensity was determined by a standard silicon photodiode. As for the light intensity-dependent measurements, the light source was a white light emitting diode, which was integrated with the Paios platform. EQE profiles were measured by a Newport Merlin lock-in amplifier.

Mobility Measurement: The structure of the hole-only devices was ITO/PEDOT:PSS/Active layer/MoO3/Ag, and the structure of the electron-only devices was ITO/ZnO/Active layer/PDINN/Ag. The mobility was determined by Paios 4.1 software with fitting the dark current to the model of single-carrier SCLC.

EQE$_{EL}$ Measurement: The EQE$_{EL}$ was recorded from a home-built system with a Hamamatsu silicon photodiode 1010B. A Keithley 2400 was used for supplying voltages and recording injected current, and a Keithley 485 for measuring the emitted light intensity.

Supporting Information

Supporting Information is available from the Wiley Online Library or from the author.

Conflict of Interest

The authors declare no conflict of interest.

Data Availability Statement

The data that support the findings of this study are available in the supplementary material of this article.

[1] C. Li, J. Zhou, J. Song, J. Xu, H. Zhang, X. Zhang, J. Guo, L. Zhu, D. Wei, G. Han, *Nat. Energy* **2021**, *6*, 605.

[2] A. J. Gillett, A. Privitera, R. Dilmurat, A. Karki, D. Qian, A. Pershin, G. Londi, W. K. Myers, J. Lee, J. Yuan, S. J. Ko, M. K. Riede, F. Gao, G. C. Bazan, A. Rao, T. Q. Nguyen, D. Beljonne, R. H. Friend, *Nature* **2021**, *597*, 666.

[3] Y. Cui, Y. Xu, H. Yao, P. Bi, L. Hong, J. Zhang, Y. Zu, T. Zhang, J. Qin, J. Ren, Z. Chen, C. He, X. Hao, Z. Wei, J. Hou, *Adv. Mater.* **2021**, *33*, e2102420.

[4] N. Ahmad, H. Q. Zhou, P. Fan, G. X. Liang, *Ecomat* **2022**, *4*, e12156.

[5] Y. Li, Y. H. Cai, Y. P. Xie, J. H. Song, H. B. Wu, Z. Tang, J. Zhang, F. Huang, Y. M. Sun, *Energy Environ. Sci.* **2021**, *14*, 5009.

[6] Y. Cai, Y. Li, R. Wang, H. Wu, Z. Chen, J. Zhang, Z. Ma, X. Hao, Y. Zhao, C. Zhang, F. Huang, Y. Sun, *Adv. Mater.* **2021**, *33*, e2101733.

[7] F. Liu, L. Zhou, W. Liu, Z. Zhou, Q. Yue, W. Zheng, R. Sun, W. Liu, S. Xu, H. Fan, L. Feng, Y. Yi, W. Zhang, X. Zhu, *Adv. Mater.* **2021**, *33*, e2100830.

[8] L. Zuo, S. B. Jo, Y. Li, Y. Meng, R. J. Stoddard, Y. Liu, F. Lin, X. Shi, F. Liu, H. W. Hillhouse, D. S. Ginger, H. Chen, A. K. Jen, *Nat. Nanotechnol.* **2022**, *17*, 53.

[9] A. Gumyusenge, D. T. Tran, X. Y. Luo, G. M. Pitch, Y. Zhao, K. A. Jenkins, T. J. Dunn, A. L. Ayzner, B. M. Savoie, J. G. Mei, *Science* **2018**, *362*, 1131.

[10] M. Nikolka, K. Broch, J. Armitage, D. Hanifi, P. J. Nowack, D. Venkateshvaran, A. Sadhanala, J. Saska, M. Mascal, S. H. Jung, J. K. Lee, I. McCulloch, A. Salleo, H. Sirringhaus, *Nat. Commun.* **2019**, *10*, 2122.

[11] D. Abbaszadeh, A. Kunz, G. A. Wetzelaer, J. J. Michels, N. I. Craciun, K. Koynov, I. Lieberwirth, P. W. Blom, *Nat. Mater.* **2016**, *15*, 628.

[12] J. Xu, S. H. Wang, G. J. N. Wang, C. X. Zhu, S. C. Luo, L. H. Jin, X. D. Gu, S. C. Chen, V. R. Feig, J. W. F. To, S. Rondeau-Gagne, J. Park, B. C. Schroeder, C. Lu, J. Y. Oh, Y. M. Wang, Y. H. Kim, H. Yan, R. Sinclair, D. S. Zhou, G. Xue, B. Murmann, C. Linder, W. Cai, J. B. H. Tok, J. W. Chung, Z. N. Bao, *Science* **2017**, *355*, 59.

[13] T. Wang, M. S. Niu, Z. C. Wen, Z. N. Jiang, C. C. Qin, X. Y. Wang, H. Y. Liu, X. Y. Li, H. Yin, J. Q. Liu, X. T. Hao, *ACS Appl. Mater. Interfaces* **2021**, *13*, 11134.

[14] T. Wang, Z.-C. Wen, L.-H. Xu, C.-C. Qin, H. Yin, J.-Q. Liu, X.-T. Hao, *J. Mater. Chem. A* **2021**, *9*, 13515.

[15] M. Wang, S. H. Liu, P. You, N. X. Wang, G. Q. Tang, Q. Miao, F. Yan, *Sol. RRL* **2020**, *4*, 2000013.

[16] J. W. Lee, B. S. Ma, H. J. Kim, T. S. Kim, B. J. Kim, *JACS Au* **2021**, *1*, 612.

[17] J. H. Han, F. Bao, D. Huang, X. C. Wang, C. M. Yang, R. Q. Yang, X. G. Jian, J. Y. Wang, X. C. Bao, J. H. Chu, *Adv. Funct. Mater.* **2020**, *30*, 2003654.

[18] J. Han, F. Bao, X. Wang, D. Huang, R. Yang, C. Yang, X. Jian, J. Wang, X. Bao, J. Chu, *Cell. Rep. Phys. Sci.* **2021**, *2*, 100408.

[19] F. Bao, J. Han, D. Huang, C. Yang, J. Wang, X. Bao, X. Jian, J. Wang, *Chem. Mater.* **2022**, *34*, 430.

[20] Y. Huang, W. Wen, S. Mukherjee, H. Ade, E. J. Kramer, G. C. Bazan, *Adv. Mater.* **2014**, *26*, 4168.

[21] J. Kniepert, I. Lange, J. Heidbrink, J. Kurpiers, T. J. K. Brenner, L. J. A. Koster, D. Neher, *J. Phys. Chem. C* **2015**, *119*, 8310.

[22] Q. Li, L.-M. Wang, S. Liu, L. Guo, S. Dong, G. Ma, Z. Cao, X. Zhan, X. Gu, T. Zhu, *ACS Energy Lett.* **2020**, *5*, 3637.

[23] Y. Cui, H. Yao, J. Zhang, T. Zhang, Y. Wang, L. Hong, K. Xian, B. Xu, S. Zhang, J. Peng, Z. Wei, F. Gao, J. Hou, *Nat. Commun.* **2019**, *10*, 2515.

[24] X. Wang, L. Zhang, L. Hu, Z. Xie, H. Mao, L. Tan, Y. Zhang, Y. Chen, *Adv. Funct. Mater.* **2021**, *31*, 2102291.

[25] H. Choi, S. J. Ko, T. Kim, P. O. Morin, B. Walker, B. H. Lee, M. Leclerc, J. Y. Kim, A. J. Heeger, *Adv. Mater.* **2015**, *27*, 3318.

[26] T. L. Nguyen, H. Choi, S.-J. Ko, M. A. Uddin, B. Walker, S. Yum, J.-E. Jeong, M. Yun, T. J. Shin, S. Hwang, *Energy Environ. Sci.* **2014**, *7*, 3040.

[27] H. Y. Fan, H. Yang, Y. Wu, O. Yildiz, X. M. Zhu, T. Marszalek, P. W. M. Blom, C. H. Cui, Y. F. Li, *Adv. Funct. Mater.* **2021**, *31*, 2103944.

[28] R. Yu, H. Yao, L. Hong, Y. Qin, J. Zhu, Y. Cui, S. Li, J. Hou, *Nat. Commun.* **2018**, *9*, 4645.

[29] R. Yu, H. Yao, Z. Chen, J. Xin, L. Hong, Y. Xu, Y. Zu, W. Ma, J. Hou, *Adv. Mater.* **2019**, *31*, e1900477.

[30] S. Bao, H. Yang, H. Fan, J. Zhang, Z. Wei, C. Cui, Y. Li, *Adv. Mater.* **2021**, *33*, e2105301.

[31] C. F. Wang, X. J. Liu, Y. Q. Xiao, J. Bergqvist, X. H. Lu, F. Gao, M. Fahlman, *Sol. RRL* **2020**, *4*, 2000261.

[32] T. X. Huang, D. F. Li, M. Ek, *Cellulose* **2018**, *25*, 2115.

[33] T. Huang, C. Chen, D. Li, M. Ek, *Cellulose* **2019**, *26*, 665.

[34] J. Yuan, Y. Zhang, L. Zhou, G. Zhang, H.-L. Yip, T.-K. Lau, X. Lu, C. Zhu, H. Peng, P. A. Johnson, *Joule* **2019**, *3*, 1140.

[35] A. Karki, J. Vollbrecht, A. L. Dixon, N. Schopp, M. Schrock, G. N. M. Reddy, T. Q. Nguyen, *Adv. Mater.* **2019**, *31*, e1903868.

[36] J. Y. Wu, J. Lee, Y. C. Chin, H. F. Yao, H. Cha, J. Luke, J. H. Hou, J. S. Kim, J. R. Durrant, *Energy Environ. Sci.* **2020**, *13*, 2422.

[37] G. Zhang, X. K. Chen, J. Xiao, P. C. Y. Chow, M. Ren, G. Kupgan, X. Jiao, C. C. S. Chan, X. Du, R. Xia, Z. Chen, J. Yuan, Y. Zhang, S. Zhang, Y. Liu, Y. Zou, H. Yan, K. S. Wong, V. Coropceanu, N. Li, C. J. Brabec, J. L. Bredas, H. L. Yip, Y. Cao, *Nat. Commun.* **2020**, *11*, 3943.

[38] N. Gasparini, X. Jiao, T. Heumueller, D. Baran, G. J. Matt, S. Fladischer, E. Spiecker, H. Ade, C. J. Brabec, T. Ameri, *Nat. Energy* **2016**, *1*, 1.

[39] S. R. Cowan, A. Roy, A. J. Heeger, *Phys. Rev. B* **2010**, *82*, 245207.

[40] L. J. A. Koster, V. D. Mihailetchi, R. Ramaker, P. W. M. Blom, *Appl. Phys. Lett.* **2005**, *86*, 123509.

[41] S. Zeiske, O. J. Sandberg, N. Zarrabi, W. Li, P. Meredith, A. Armin, *Nat. Commun.* **2021**, *12*, 3603.

[42] U. Rau, *Phys. Rev. B* **2007**, *76*, 085303.